

Quantitative Measurement of Metal Accumulation in Brain of Patients With Wilson's Disease

Gaiying Li, PhD,¹ Rong Wu, MD,² Rui Tong, MS,¹ Binshi Bo, MS,¹ Yu Zhao, MS,¹ Kelly M. Gillen, PhD,³ Pascal Spincemaille, PhD,³ Yixuan Ku, PhD,⁴ Yasong Du, MD,⁵ Yi Wang, PhD,³ Xiaoping Wang, MD, PhD,^{2*} and Jianqi Li, PhD^{1*}

¹Shanghai Key Laboratory of Magnetic Resonance, School of Physics and Electronic Science, East China Normal University, Shanghai, China

²Department of Neurology, Shanghai Tong-Ren Hospital, Shanghai Jiao Tong University School of Medicine, Shanghai, China

³Department of Radiology, Weill Medical College of Cornell University, New York, New York, USA

⁴Department of Psychology, Sun Yat-sen University, Guangzhou Higher Education Mega Center, Guangzhou, China

⁵Shanghai Mental Health Center, Shanghai Jiao Tong University School of Medicine, Shanghai, China

ABSTRACT: Background: Currently, no study has evaluated metal accumulation in the brains of patients with Wilson's disease by using quantitative susceptibility mapping at 3T MRI. The objectives of this study were to qualitatively and quantitatively evaluate changes in magnetic susceptibility and R2* maps in deep gray matter nuclei to discriminate Wilson's disease patients from healthy controls and to evaluate their sensitivities in diagnosing Wilson's disease.

Methods: Magnetic susceptibility and R2* maps and conventional T1-weighted, T2-weighted, and T2-weighted fluid-attenuated inversion recovery images were obtained from 17 Wilson's disease patients and 14 age-matched healthy controls on a 3T MRI scanner. Differences between Wilson's disease and healthy control groups in susceptibility and R2* values in multiple deep nuclei were evaluated using a Mann-Whitney *U* test and receiver operating characteristic curves. The correlations of susceptibility and R2* values with Unified Wilson's Disease Rating Scale score were also performed.

Results: Magnetic susceptibility and R2* can effectively distinguish different types of signal abnormalities. Magnetic susceptibility and R2* values in multiple deep nuclei of Wilson's disease patients were significantly higher than those in healthy controls. Magnetic susceptibility value in the substantia nigra had the highest area under the curve (0.888). There were positive correlations of the Unified Wilson's Disease Rating Scale score with susceptibility values in the caudate nucleus ($r = 0.757$, $P = 0.011$), putamen ($r = 0.679$, $P = 0.031$), and red nucleus ($r = 0.638$, $P = 0.047$), as well as R2* values in the caudate nucleus ($r = 0.754$, $P = 0.012$).

Conclusions: Quantitative susceptibility mapping at 3T could be a useful tool to evaluate metal accumulation in deep gray matter nuclei of Wilson's disease patients. © 2020 International Parkinson and Movement Disorder Society

Key Words: deep gray matter nuclei; quantitative susceptibility mapping; R2* mapping; Wilson's disease

Wilson's disease (WD) is an autosomal-recessive disorder characterized by abnormal accumulation of

copper and iron in many tissues, especially in the liver and brain, resulting in severe disability and death if

*Correspondence to: Jianqi Li, PhD, Shanghai Key Laboratory of Magnetic Resonance, School of Physics and Electronic Science, East China Normal University, 3663 North Zhongshan Road, Shanghai 200062, China; E-mail: jqli@phy.ecnu.edu.cn. Xiaoping Wang, MD, PhD, Department of Neurology, Shanghai Tong-Ren Hospital, Shanghai Jiao Tong University School of Medicine, 1111 Xianxia Road, Shanghai, 200080, China; E-mail: wangxp@ustc.edu.

Gaiying Li and Rong Wu contributed equally to the work of this article.

Relevant conflicts of interest/financial disclosures: Y.W. owns equity of Medimagetric LLC, a Cornell spinoff company. No other author has a conflict of interest to declare.

Funding agencies: This study was supported in part by grants from the National Natural Science Foundation of China (grant numbers 81271533, 81671103), the Social Science Foundation of China (grant number 15ZDB016).

Received: 18 January 2020; **Revised:** 12 May 2020; **Accepted:** 18 May 2020

Published online 00 Month 2020 in Wiley Online Library (wileyonlinelibrary.com). DOI: 10.1002/mds.28141

untreated.¹⁻⁴ WD is caused by a mutation in the *ATP7B* gene, which encodes the enzyme ATPase 2, a transport protein that eliminates copper from the liver via bile and plasma. Mutations in *ATP7B* lead to reduced copper efflux and reduced serum ceruloplasmin. Because ceruloplasmin is also a ferroxidase enzyme, its reduced levels can cause disruptions in iron metabolism.⁵⁻⁷ Excess metals can cause toxicity, which results in damage to neurons and astrocytes and has been implicated in many other neurodegenerative processes.⁸⁻¹⁰

WD diagnosis can be easily overlooked, but if it is diagnosed early, effective treatments are available to prevent or reverse tissue and organ damages.¹⁻¹⁰ Diagnosis of WD can be challenging because WD symptoms are often nonspecific and can be confused with other liver diseases such as hepatitis. Patients with neurological symptoms can be diagnosed easily. The presence of neurological symptoms is related to abnormal neuroimaging findings, such as a hyperintense signal in putaminal lesions on T2-weighted (T2-w) images in magnetic resonance imaging (MRI) of all symptomatic patients.^{11,12} MRI may catch brain tissue damage before neurological symptom manifestation,^{9,13} which is helpful for early diagnosis. Therefore, MRI can be a particularly important tool for capturing WD's neurological consequences.

There have been few studies evaluating the sensitivity of various MRI sequences in WD patients. In patients with WD who have neurological symptoms, conventional T2-w images showed hyperintensities of the globus pallidus (GP), corpus striatum, and brain stem that correlate with neurologic symptoms. Conversely, hyperintensities of the bilateral GP on T1-weighted (T1-w) images may be detected before neurologic impairment.^{14,15} A recent postmortem study in WD demonstrated that R2* values correlated with iron content in the GP and putamen (PUT) using 7T.⁷ However, R2* mapping depends on factors such as field strength and inhomogeneity of iron distribution, and contains substantial blooming artifacts that increase with echo time (TE) and depend on head orientation.^{16,17}

Tissue magnetic susceptibility, which directly reflects the molecular electron cloud behavior in the main magnetic field, can be measured using the widely available gradient echo (GRE) sequence. Quantitative susceptibility mapping (QSM)¹⁸ can deconvolve the blooming artifacts in GRE phase data to determine tissue magnetic susceptibility distribution¹⁹⁻²¹ by identifying the magnetic field induced by tissue susceptibility²² and solving the field-to-susceptibility source inverse problem.^{17,23-27} QSM has promising clinical and scientific applications that involve changes in metal content by hemoglobin, ferritin, calcification, and contrast agents.^{18,28-31}

Previous studies found increased susceptibility values in patients with WD in cerebral tissue, using a 1.5T

scanner with limited image quality or a 7T scanner with superior image quality but scarce clinical availability.^{9,32,33} Even though 3T MRI is commonly used in the clinic, there is no study on WD using QSM on a 3T scanner.

We hypothesized that *in vivo* QSM on readily available 3T scanners can be used to quantify brain metal accumulation in patients with WD. In this study, we first evaluated signal appearance of the deep gray matter nuclei in QSM in combination with conventional MRI. Then, we quantitatively evaluated changes in magnetic susceptibility and R2* values in deep gray matter nuclei to discriminate patients with WD from healthy controls (HCs) and compare the sensitivity of QSM and R2* maps in the diagnosis of WD. Furthermore, we correlated the clinical manifestation of WD with magnetic susceptibility and R2* values.

Materials and Methods

Study Subjects

This prospective study was approved by the local ethical committee, and all participants signed an informed consent form. From December 2014 until May 2015, 17 patients with WD and 14 HCs were recruited to participate in this 3T MRI study. The diagnostic criteria for WD patients were based on the Wilson's disease scoring system mentioned in the European Association for the Study of the Liver Clinical Practice Guidelines: Wilson's disease.^{34,35} The diagnostic scores were based on all available tests, including Kayser-Fleischer rings, neurologic symptoms, serum ceruloplasmin, Coombs-negative hemolytic anemia, and urinary copper (in the absence of acute hepatitis). Neurological symptoms were evaluated using the Unified Wilson's Disease Rating Scale (UWDRS) at the time of diagnosis.³⁶ The scoring system is summarized in Table S1. A patient was diagnosed with WD if the total score was 4 or more. The exclusion criteria were as follows: history of other neurological and psychiatric disorders or any other hepatic disease, WD as a secondary disease.

Patients were evaluated for the presence of any neurologic findings by 2 neurologists (R.W., 5 years of experience; X.P.W., >30 years of experience). All HCs had no history of neurological diseases by neuropathological examination and no decreased serum ceruloplasmin or increased urinary copper excretion. All subjects were right-handed.

Imaging Acquisition

All participants were scanned on a clinical 3T MR imaging system (Magnetom Trio Tim, Siemens Healthcare, Erlangen, Germany) equipped with a 12-channel head matrix coil. During scanning, foam pads were placed around each subject's head to minimize

head motion. Magnetic susceptibility and $R2^*$ maps were generated from the same 3-D spoiled multiecho GRE sequence with the following parameters: TR, 60 milliseconds; TE1, 6.8 milliseconds; ΔTE , 6.8 milliseconds; echo number, 8; flip angle, 15° ; FOV, $240 \times 180 \text{ mm}^2$; in-plane resolution, $0.625 \times 0.625 \text{ mm}^2$; slice thickness, 2 mm; number of slices, 96. In addition, a generalized autocalibrating partially parallel acquisition with an acceleration factor of 2 in the right-left direction and elliptical sampling were used to reduce acquisition time. Standard T1-w, T2-w, and T2-weighted fluid-attenuated inversion recovery (FLAIR) images were also obtained. T1-w images were acquired using a spin echo sequence with TR, 450 milliseconds; TE, 9 milliseconds; FOV, $240 \times 180 \text{ mm}^2$; matrix, 256×192 ; slice thickness, 4 mm; slice number, 30. T2-w images were acquired using a fast-spin echo sequence with TR, 6000 milliseconds; TE, 93 milliseconds; FOV, $240 \times 180 \text{ mm}^2$; matrix, 320×240 ; slice thickness, 4 mm; slice number, 30. T2-weighted FLAIR images were obtained using the following parameters: TR, 9000 milliseconds; TE, 93 milliseconds; TI, 2500 milliseconds; FOV, $220 \times 200 \text{ mm}^2$; matrix, 256×232 ; slice thickness, 4 mm; slice number, 25.

Before the QSM and $R2^*$ reconstructions, 2 researchers independently graded the quality of the magnitude images: 1 = very good (few or no artifacts); 2 = good (visible artifacts); 3 = poor (considerable motion artifacts); 4 = very poor (significant motion artifacts); 5 = non-diagnostic scan. Subjects with a consensus grading score higher than 2 were excluded from further analysis.

Data Processing

QSM maps were reconstructed using the morphology-enabled dipole inversion (MEDI) toolbox (<http://pre.weill.cornell.edu/mri/pages/qsm.html>). The field map was first estimated by performing a 1-dimensional temporal unwrapping of the phase on each voxel followed by a weighted least-squares fit of the temporally unwrapped phases in each voxel over TE.²⁵ To account for frequency aliasing on the field map, a magnitude map-guided spatial unwrapping algorithm was applied.³⁷ The background field was removed using the projection onto dipole fields method.³⁸ Finally, the remaining tissue field was inverted to generate a susceptibility map using the MEDI with automatic uniform cerebrospinal fluid (CSF) zero reference algorithm,³⁹ which added regularization in the QSM reconstruction to suppress ventricular CSF susceptibility inhomogeneity.⁴⁰ CSF instead of white matter was used as the susceptibility reference region to avoid any potential errors caused by the susceptibility anisotropy effect of white matter and to exclude any influence of potential iron and copper deposition within white matter.⁴¹ $R2^*$ maps were reconstructed from the magnitude gradient-

echo data with a monoexponential fit using the Levenberg-Marquart algorithm.

Previous studies in WD with conventional MRI, susceptibility-weighted imaging, and QSM revealed that signal abnormality presented in not only the basal ganglia, but also the substantia nigra (SN), red nucleus (RN), and dentate nucleus (DN).⁴²⁻⁴⁴ In addition, a postmortem study demonstrated metal accumulation in these regions in patients with WD.⁴⁵ Therefore, these 6 regions of interest (ROIs) were selected to measure metal deposition. ROIs were drawn manually on the QSM images using insight toolkit-snake automatic partitioning software (<http://www.itksnap.org>) by 2 researchers who were blinded to subject demographics. The ROIs were drawn to cover the bilateral nuclei in all sections in which the deep nucleus was visible (Fig. S1). In the basal ganglia region, we avoided patchy areas with hypointense signal, which was suspected edema. To minimize partial volume effects, these sections never included the most inferior or superior slice on which the nucleus was defined. Voxels at the tissue boundaries were also excluded. ROIs were confirmed by a neurologist (XP.W.). To maintain accuracy in quantitative evaluations, the ROIs drawn on the QSM images were applied to $R2^*$ maps.

Qualitative Analyses

Two researchers independently evaluated the signal abnormality of all images. The signal intensity abnormalities in the images of patients with WD were divided into 3 types in conventional MRI images: type I showed hypointensity on T2-w and FLAIR images; type II showed patchy hypointense regions on T1-w images and patchy hyperintense regions on T2-w and FLAIR images; type III consisted of some hypointense pixels on FLAIR images, but hyperintensity on T2-w images. The signal characteristic of the 3 types of lesions in susceptibility and $R2^*$ maps were also evaluated.

Statistical Analyses

A possible influence of sex between groups was evaluated using a chi-square test, interobserver variability of the visual evaluation was evaluated using a kappa test, and the influence of age was tested by 1-way analysis of variance. Interobserver segmentation variability was tested using the intraclass correlation coefficient (ICC) for the 2 researchers. An ICC of 0.81 to 1.00 was considered excellent agreement.

Differences in magnetic susceptibility and $R2^*$ values between WD patients and HCs were compared using the Mann-Whitney U test. Multiple comparisons were corrected using the false discovery rate correction.⁴⁶ Adjusted $P < 0.05$ was chosen to designate significant differences. Associations of magnetic susceptibility and $R2^*$ values with UWDRS scores were assessed by calculating

the partial correlation coefficient. Receiver operating characteristic (ROC) curves were used to assess the ability of QSM and $R2^*$ maps to discriminate between WD and HCs. Sensitivity and specificity were determined by Youden index. The predictive capability of QSM and $R2^*$ was assessed using the area under the curve (AUC). The value of the AUC varied from 0.5 to 1.0, with higher values corresponding to a greater ability to distinguish between the 2 groups. Diagnostic accuracy of qualitative and quantitative analysis in each region was calculated.

All statistical analyses were carried out using IBM SPSS Statistics 23 and MATLAB R2010b (MathWorks, MA).

Results

Subject Characteristics

Three WD patients were excluded because of motion artifacts. A total of 14 WD patients (10 men and 4 women) with a mean age of 28.1 ± 9.6 years and 14

age- and sex-matched HCs (9 men and 5 women) with a mean age of 28.2 ± 9.2 years were included for further analysis. The median duration of illness was 27 months (range, 4–312 months). Clinical and demographic parameters of WD patients are summarized in Table S2. There were no significant differences between the WD and HC groups with respect to age ($F = 0.002$, $P = 0.968$, $\eta_p^2 < 0.001$) or sex ($\chi^2 = 0.164$, $P = 0.686$, $\phi = 0.076$).

MRI Findings

Ten patients with WD (71%) had signal abnormalities in the lenticular nucleus (GP and PUT) in conventional MR images (Fig. 1). All 10 (100%) had type I lesions (Fig. 1d,g), whereas 3 patients (30%) had type II lesions (Fig. 1b,e,h) and 6 patients (60%) had type III lesions (Fig. 1f,i).

There was high contrast between deep gray matter nuclei and the surrounding tissue in both susceptibility and $R2^*$ maps. The signal intensity of lesions in

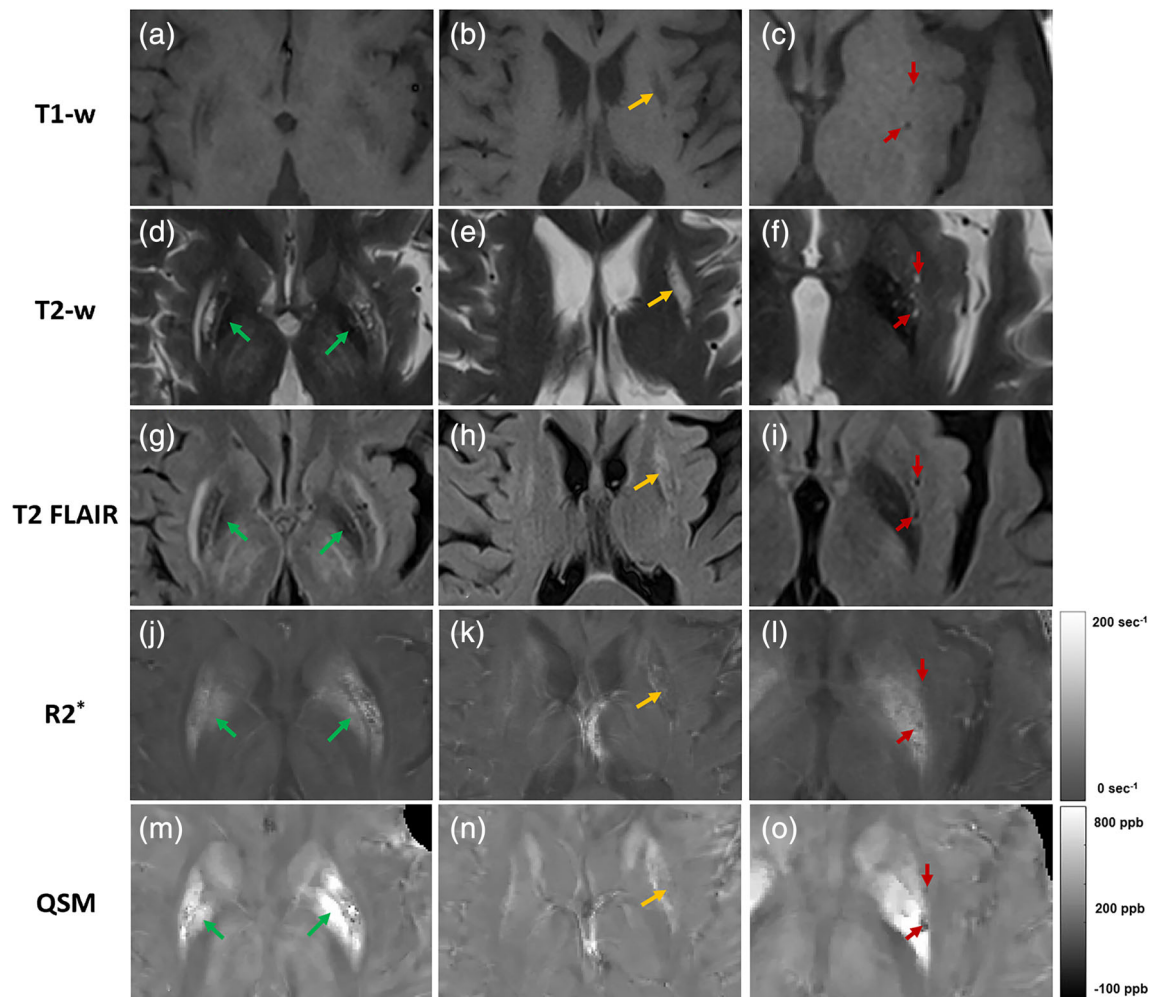


FIG 1 Representative T1-w, T2-w, T2 FLAIR, $R2^*$ and QSM images of the lenticular nuclei from WD patients. Note signal abnormalities in type I (green arrow in left column), type II (yellow arrow in middle column), and type III (red arrow in right column). [Color figure can be viewed at wileyonlinelibrary.com]

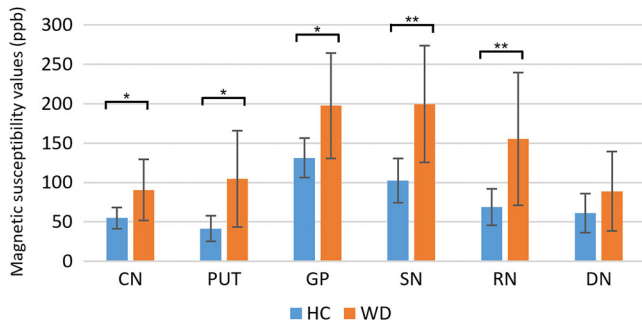


FIG 2 Comparison of mean susceptibility values between patients with WD and HC in the bilateral head of the caudate nucleus (CN), putamen (PUT), globus pallidus (GP), substantia nigra (SN), red nucleus (RN), and dentate nucleus (DN). Significant differences between WD and HC are represented as: * $P < 0.05$; ** $P < 0.01$. Error bar: \pm SD. [Color figure can be viewed at wileyonlinelibrary.com]

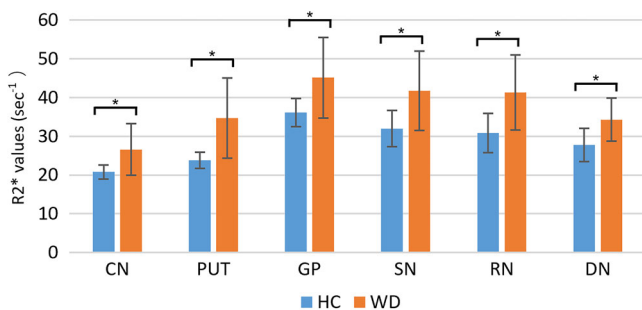


FIG 3 Comparison of mean $R2^*$ values between WD and HC in the bilateral head of the caudate nucleus (CN), putamen (PUT), globus pallidus (GP), substantia nigra (SN), red nucleus (RN), and dentate nucleus (DN). Significant differences between WD and HC are represented as: * $P < 0.05$; ** $P < 0.01$. Error bar: \pm SD. [Color figure can be viewed at wileyonlinelibrary.com]

susceptibility and $R2^*$ maps changed with the type of lesion. The type I lesions showed hyperintensity in both susceptibility and $R2^*$ maps (Fig. 1m,j). The type II lesions showed patchy regions with susceptibility and $R2^*$ values close to those of the surrounding white matter (Fig. 1n,k). The type III lesions were presented as some hypointense pixels in both susceptibility and $R2^*$ maps (Fig. 1o,l). Diagnostic accuracy based on qualitatively visual assessment was 82.14% in both QSM and $R2^*$.

A high degree of interrater reliability was determined using Kappa's coefficient, with $\kappa = 0.858$ for QSM and $\kappa = 0.667$ for $R2^*$.

Test-Retest Reliability Analysis

Test-retest reliability of manual ROI voxel volume extraction by 2 researchers was evaluated using ICC analysis. The maximum ICC value was 0.95 in the DN, and the smallest ICC was 0.85 in the RN, indicating excellent interobserver agreement for all ROIs. Given the excellent agreement between the 2 researchers, the

TABLE 1 Results of the ROC curve analyses of QSM and $R2^*$ images between healthy controls and patients with Wilson's disease

		AUC	SS	SP	<i>P</i>	AC (%)
QSM	CN	0.806	64.29	92.86	0.006	78.57
	PUT	0.781	71.43	100.00	0.012	85.71
	GP	0.786	64.29	85.71	0.010	75.00
	SN	0.888	85.71	92.86	<0.001	89.29
	RN	0.857	78.57	100.00	0.001	89.29
	DN	0.776	64.29	100.00	0.013	82.14
$R2^*$	CN	0.776	64.29	100.00	0.013	82.14
	PUT	0.781	71.43	100.00	0.012	85.71
	GP	0.735	57.14	100.00	0.035	78.57
	SN	0.791	64.29	92.86	0.009	78.57
	RN	0.811	85.71	71.43	0.005	78.57
	DN	0.837	78.57	85.71	0.002	82.14

Note: Results of the ROC curve analyses are expressed by area under the ROC curve (AUC), sensitivity (SS), specificity (SP), *P* value, and diagnostic accuracy (AC); only statistically significant differences in ROC curve analyses between the HC and WD groups are shown.

results of the susceptibility and $R2^*$ values were the average of the 2 researchers' measurements.

ROI Analysis on QSM and $R2^*$ Maps

In all subjects, the deep gray matter nuclei were more apparent and clearer in susceptibility maps than in the $R2^*$ maps (Fig. S2). After correction for multiple comparisons, susceptibility values in patients with WD were significantly higher than those of HCs in the CN ($P = 0.010$), PUT ($P = 0.013$), GP ($P = 0.013$), SN ($P = 0.001$), and RN ($P = 0.002$). However, susceptibility values did not significantly differ in the DN between patients with WD and HCs ($P = 0.150$; Fig. 2).

For all regions measured, there were significantly higher $R2^*$ values in patients with WD than in HCs: CN ($P = 0.014$), PUT ($P = 0.014$), GP ($P = 0.035$), SN ($P = 0.014$), RN ($P = 0.012$), and DN ($P = 0.012$); see Figure 3.

ROC Curve Analysis on QSM and $R2^*$ Maps

The results of ROC curve analyses of QSM and $R2^*$ maps between HCs and WD are summarized in Figure S3 and Table 1. For QSM, AUC for the mean susceptibility in the CN, PUT, GP, SN, and RN were 0.806 ($P = 0.006$), 0.781 ($P = 0.012$), 0.786 ($P = 0.010$), 0.888 ($P < 0.001$), and 0.857 ($P = 0.001$), respectively, demonstrating that QSM in the SN was better than that of other regions at classifying WD patients. For $R2^*$, the AUC in the CN, PUT, GP, SN, RN, and DN were 0.776 ($P = 0.013$), 0.781 ($P = 0.012$), 0.735 ($P = 0.009$), 0.791 ($P = 0.035$), 0.811 ($P = 0.005$), and 0.837 ($P = 0.002$), respectively, indicating that the RN provided the highest AUC value at classifying WD patients. Taken together, QSM provided the highest AUC value of 0.888 in the SN. Midbrain nuclei (SN and RN) showed better performance than basal ganglia nuclei (CN, PUT, and GP) and

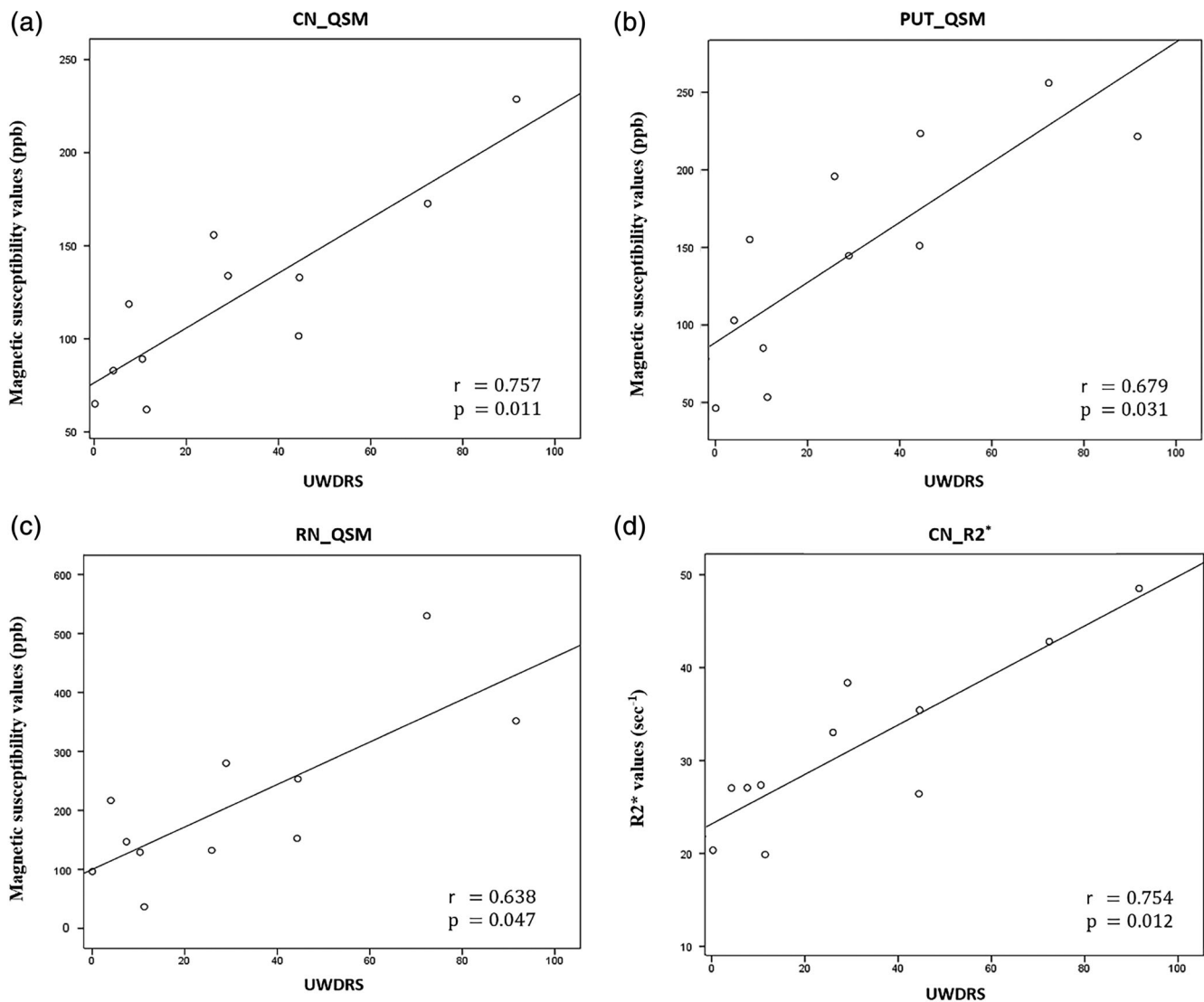


FIG 4 In the patients with WD, magnetic susceptibility values in the caudate nucleus (CN) (a), putamen (PUT) (b) and red nucleus (RN) (c), as well as R2* values (d) in the CN increased with the severity of neurological symptoms.

cerebellum (DN) in both QSM and R2* for this study. The AUC values in the midbrain nuclei by QSM were higher than those by R2*, but there was no significant difference between the AUC of QSM and R2* in the SN ($z = 1.655$, $P = 0.098$) or the RN ($z = 0.833$, $P = 0.405$) regions.

The results of diagnostic accuracy for each nucleus on QSM and R2* are summarized in Table 1. The magnetic susceptibility in the SN and RN showed the highest diagnostic accuracy (89.28 %).

Correlation Analysis

Finally, we examined the correlation of QSM and R2* values in the deep gray matter nuclei with clinical index in WD subjects. After sex was assigned as a covariate, there was a positive correlation between susceptibility value and UWDRS score in the CN

($r = 0.757$, $P = 0.011$), PUT ($r = 0.679$, $P = 0.031$), and RN ($r = 0.638$, $P = 0.047$); see Figure 4a–c. No such correlation was found in the GP ($r = 0.519$, $P = 0.102$), SN ($r = 0.321$, $P = 0.366$), and DN ($r = 0.521$, $P = 0.123$). For the R2* values, there was a correlation only between R2* in the CN and UWDRS ($r = 0.754$, $P = 0.012$; Fig. 4d), but not in the PUT ($r = 0.539$, $P = 0.108$), GP ($r = 0.589$, $P = 0.073$), SN ($r = 0.004$, $P = 0.991$), RN ($r = 0.149$, $P = 0.682$), or DN ($r = 0.267$, $P = 0.457$). In addition, there was no correlation of QSM or R2* values with other clinical indices, notably urinary copper and serum ceruloplasmin.

Discussion

In this exploratory study, we qualitatively and quantitatively investigated the signal abnormalities of the

bilateral CN, GP, PUT, SN, RN, and DN in terms of both susceptibility and $R2^*$ maps on a 3T MRI. Both QSM and $R2^*$ showed manifestations of abnormal values in these deep gray matter nuclei. Significantly increased magnetic susceptibility and $R2^*$ values were observed in multiple brain regions of patients with WD. Moreover, the measured magnetic susceptibility values in multiple regions increased with the severity of neurological symptoms. In terms of group differences, classification power, diagnostic accuracy, and ability to correlate with clinical scores, QSM performed better than $R2^*$. Therefore, QSM from a 3T scanner may provide useful information for diagnosis of WD patients.

Compared with QSM studies of differentiating the deposition of iron and copper in the lenticular nucleus in WD patients from HCs at 1.5T,^{9,33} this QSM study on a clinical 3T MRI scanner indicated greater statistical power (P values approximately reduced by a factor of 10), approaching that at 7T.³² It is known that QSM at 3T is superior to QSM at 1.5T in terms of signal-to-noise ratio efficiency.²⁷ Technical optimization may be needed to take full advantage of QSM at 7T.⁴⁷ This comparison should be understood with the limitation that the WD patient cohorts are different among these studies. Nevertheless, our results suggest that QSM at 3T is potentially a clinically useful tool for WD diagnosis.

Three types of lesions in the lenticular nucleus could be identified by QSM and $R2^*$. In patients with WD, excess copper is initially taken up and buffered by astrocytes and oligodendrocytes but ultimately causes dysfunction of the blood-brain barrier and demyelination. The most severe neuropathologic abnormalities, including tissue rarefaction, reactive astrogliosis, myelin pallor, and the presence of iron-laden macrophages, are typically present in the putamen and other nuclei in the basal ganglia. In this study, the presence of type I lesions was most likely because of excessive metal deposition. The accumulation of paramagnetic metal may increase the susceptibility values in tissue and further dephase the MR signals, resulting in hypointense signals in T2-w and FLAIR images. Type II lesions were likely because of edema.⁴⁸ Edema has a susceptibility value similar to that of white matter, and long T1 and T2 values because of edema cause hypointense signals in T1-w images and hyperintense signals in T2-w images. Type III lesions could reflect encephalomalacia. The susceptibility of encephalomalacia is similar to that of CSF, which shows a lower susceptibility value than the surrounding deep nuclei, hypointense signal in T1-w, hyperintense signal in T2-w, and suppressed signal in FLAIR images. Taken together, both QSM and $R2^*$ performed well in distinguishing different types of lesions in WD patients, which provide auxiliary information for WD diagnosis.

Based on the quantitative results in group difference, classification power, diagnostic accuracy, and ability to correlate with clinical scores, QSM was relatively

superior to $R2^*$ in distinguishing patients with WD from HCs. This may be because QSM is a direct calculation of the magnetic susceptibility distribution.⁴⁹⁻⁵¹ However, many factors, such as changes in water content, local water diffusion rates in an inhomogeneous field, macroscopic magnetic field's inhomogeneity and nonlocality, and imaging parameters including field strength, voxel size, and TE,^{16,52} can all confound the interpretation of $R2^*$ mapping, resulting in a complicated relationship to iron concentration that may be quadratic rather than linear.⁵³ These effects could reduce the sensitivity of $R2^*$ mapping. Therefore, experimental and theoretical findings support the notion that QSM can overcome the problems of $R2^*$ and reflect spatial variation in tissue composition,⁵⁴⁻⁵⁶ thus providing a relatively accurate tool for measuring magnetic susceptibility changes.

For the first time, a significant positive correlation between the UWDRS score of the WD group and susceptibility values were observed in the CN, PUT, and RN. These findings suggest that patients with higher metal accumulation in these nuclei may correspond to higher scores of neurological symptoms. In a previous postmortem study, the degree of pathological severity in the putamen of WD revealed a trend for a positive association with iron concentration.⁴⁵ Therefore, the susceptibility values in the deep gray matter nuclei might be an acceptable noninvasive biomarker for WD progression.

This work represents a preliminary analysis of QSM and $R2^*$ at 3T MRI to distinguish patients with WD from HCs. The following limitations could be overcome in additional studies: First, statistical power was limited because of the small number of subjects. A larger sample size would be required to validate and refine the present work. Second, a previous study showed that there are different disease manifestations that may result in differences in metal accumulation.³² In this study, we did not separate WD subjects into hepatic, neurological, or neuropsychiatric subgroups because of the small sample size. Third, susceptibility values in patients with WD were higher than those in HCs in the DN, but the difference was not statistically significant. That may be because there was a higher SD value in this region. Therefore, further investigations on metal accumulation in the DN are needed. Finally, because of the strong contrast of the QSM in the deep gray matter nuclei, we focused on QSM of the deep gray matter nuclei and did not include the brain stem and pons, noting that these are known to be involved in clinically affected neuronal circuits in WD.

Conclusion

Abnormal metal accumulation in multiple deep gray matter nuclei of patients with WD could be detected

quantitatively and qualitatively using both QSM and $R2^*$ at 3T MRI. QSM performed relatively better than $R2^*$ in terms of group differences, classification power, diagnostic accuracy, and ability to correlate with clinical scores in this study. In summary, QSM at 3T could be an effective tool to evaluate metal accumulation in the brains of patients with WD. ■

Acknowledgments: This study was supported by Microscale Magnetic Resonance Platform of ECNU.

References

- Ala A, Walker AP, Ashkan K, Dooley JS, Schilsky ML. Wilson's disease. *Lancet* 2007;369(9559):397–408.
- Litwin T, Gromadzka G, Szpak GM, Jablonka-Salach K, Bulska E, Czlonkowska A. Brain metal accumulation in Wilson's disease. *J Neurol Sci* 2013;329(1-2):55–58.
- Pfeiffer R. Wilson's Disease. *Sem Neurol* 2007;27(2):123–132.
- Roberts EA, Schilsky ML. Diagnosis and treatment of Wilson disease: An update. *Hepatology* 2008;47(6):2089–2111.
- Brewer GJ. Risks of Copper and Iron Toxicity during Aging in Humans. *Chem Res Toxicol* 2010;23(2):319–326.
- Pfeiffenberger J, Gotthardt DN, Herrmann T, et al. Iron metabolism and the role of HFE gene polymorphisms in Wilson disease. *Liver Int* 2012;32(1):165–170.
- Dusek P, Bahn E, Litwin T, et al. Brain iron accumulation in Wilson disease: a post mortem 7 Tesla MRI - histopathological study. *Neuropathol Appl Neurobiol* 2017;43(6):514–532.
- Sekler I, Silverman WF. Zinc homeostasis and signaling in glia. *Glia* 2012;60(6):843–850.
- Saracoglu S, Gumus K, Doganay S, Koc G, Kacar Bayram A, Arslan D, et al. Brain susceptibility changes in neurologically asymptomatic pediatric patients with Wilson's disease: evaluation with quantitative susceptibility mapping. *Acta Radiol* 2018;028418511875982.
- Li WJ, Chen C, You ZF, Yang RM, Wang XP. Current Drug Managements of Wilson's Disease: From West to East. *Curr Neuropharmacol* 2016;14(4):322–325.
- Grimm G, Prayer L, Oder W, et al. Comparison of functional and structural brain disturbances in Wilson's disease. *Neurology* 1991;41(2 (Pt 1)):272–76.
- Magalhaes AC, Caramelli P, Menezes JR, et al. Wilson's disease: MRI with clinical correlation. *Neuroradiology* 1994;36(2):97–100.
- Davatzikos C, Fan Y, Wu X, Shen D, Resnick SM. Detection of prodromal Alzheimer's disease via pattern classification of magnetic resonance imaging. *Neurobiol Aging* 2008;29(4):514–523.
- Roh JK, Lee TG, Wie BA, Lee SB, Park SH, Chang KH. Initial and follow-up brain MRI findings and correlation with the clinical course in Wilson's disease. *Neurology* 1994;44(6):1064.
- Kim TJ, Kim IO, Kim WS, et al. MR imaging of the brain in Wilson disease of childhood: Findings before and after treatment with clinical correlation. *Am J Neuroradiol* 2006;27(6):1373–378.
- Li J, Chang S, Liu T, et al. Reducing the object orientation dependence of susceptibility effects in gradient echo MRI through quantitative susceptibility mapping. *Magn Reson Med* 2012;68(5):1563–1569.
- Bilgic B, Pfefferbaum A, Rohlfing T, Sullivan EV, Adalsteinsson E. MRI estimates of brain iron concentration in normal aging using quantitative susceptibility mapping. *Neuroimage* 2012;59(3):2625–2635.
- de Rochefort L, Liu T, Kressler B, et al. Quantitative Susceptibility Map Reconstruction from MR Phase Data Using Bayesian Regularization: Validation and Application to Brain Imaging. *Magn Reson Med* 2010;63(1):194–206.
- Haacke EM, Liu S, Buch S, Zheng W, Wu D, Ye Y. Quantitative susceptibility mapping: current status and future directions. *Magn Reson Imaging* 2015;33(1):1–25.
- Wang Y, Liu T. Quantitative susceptibility mapping (QSM): Decoding MRI data for a tissue magnetic biomarker. *Magn Reson Med* 2015;73(1):82–101.
- Liu CL, Li W, Tong KA, Yeom KW, Kuzminski S. Susceptibility-weighted imaging and quantitative susceptibility mapping in the brain. *J Magn Reson Imaging* 2015;42(1):23–41.
- Zhou D, Liu T, Spincemaille P, Wang Y. Background field removal by solving the Laplacian boundary value problem. *NMR Biomed* 2014;27(3):312–319.
- Kee Y, Liu Z, Zhou L, et al. Quantitative Susceptibility Mapping (QSM) Algorithms: Mathematical Rationale and Computational Implementations. *IEEE Trans Biomed Eng* 2017;64(11):2531–2545.
- Langkammer C, Schweser F, Krebs N, et al. Quantitative susceptibility mapping (QSM) as a means to measure brain iron? A post mortem validation study. *Neuroimage* 2012;62(3):1593–1599.
- Liu T, Eskreis-Winkler S, Schweitzer AD, et al. Improved Subthalamic Nucleus Depiction with Quantitative Susceptibility Mapping. *Radiology* 2013;269(1):216–223.
- Liu Z, Kee Y, Zhou D, Wang Y, Spincemaille P. Preconditioned total field inversion (TFI) method for quantitative susceptibility mapping. *Magn Reson Med* 2017;78(1):303–315.
- Deh K, Nguyen TD, Eskreis-Winkler S, et al. Reproducibility of quantitative susceptibility mapping in the brain at two field strengths from two vendors. *J Magn Reson Imaging* 2015;42(6):1592–1600.
- Schweser F, Deistung A, Lehr BW, Reichenbach JR. Differentiation between diamagnetic and paramagnetic cerebral lesions based on magnetic susceptibility mapping. *Med Phys* 2010;37(10):5165–178.
- Wharton S, Schäfer A, Bowtell R. Susceptibility mapping in the human brain using threshold-based k-space division. *Magn Reson Med* 2010;63(5):1292–304.
- Versluis MJ, van der Grond J, van Buchem MA, van Zijl P, Webb AG. High-Field Imaging of Neurodegenerative Diseases. *Neuroimaging Clin N Am* 2012;22(2):159–171.
- Wang Y, Spincemaille P, Liu Z, et al. Clinical quantitative susceptibility mapping (QSM): Biometal imaging and its emerging roles in patient care. *J Magn Reson Imaging* 2017;46(4):951–971.
- Fritzsche D, Reiss-Zimmermann M, Trampel R, Turner R, Hoffmann KT, Schafer A. Seven-Tesla Magnetic Resonance Imaging in Wilson Disease Using Quantitative Susceptibility Mapping for Measurement of Copper Accumulation. *Invest Radiol* 2014;49(5):299–306.
- Doganay S, Gumus K, Koc G, et al. Magnetic Susceptibility Changes in the Basal Ganglia and Brain Stem of Patients with Wilson's Disease: Evaluation with Quantitative Susceptibility Mapping. *Magn Reson Med Sci* 2018;17(1):73–79.
- European Association for Study of L. EASL Clinical Practice Guidelines: Wilson's disease. *J Hepatol* 2012;56(3):671–685.
- Ferenci P, Caca K, Loudianos G, et al. Diagnosis and phenotypic classification of Wilson disease. *Liver Int* 2003;23(3):139–142.
- Czlonkowska A, Tarnacka B, Moller JC, et al. Unified Wilson's Disease Rating Scale (UWDRS) — a proposal for the neurological scoring of Wilson's disease patients. *Parkinsonism Relat Disord* 2007;13:S80–S.
- Cusack R, Papadakis N. New robust 3-D phase unwrapping algorithms: Application to magnetic field mapping and undistorting echoplanar images. *Neuroimage* 2002;16(3):754–764.
- Liu T, Khalidov I, de Rochefort L, Spincemaille P, Liu J, Tsiouris AJ, et al. A novel background field removal method for MRI using projection onto dipole fields (PDF). *NMR Biomed* 2011;24(9):1129–1136.
- Liu Z, Spincemaille P, Yao Y, Zhang Y, Wang Y. MEDI+0: Morphology enabled dipole inversion with automatic uniform cerebrospinal fluid zero reference for quantitative susceptibility mapping. *Magn Reson Med* 2018;79(5):2795–803.
- Liu T, Xu WY, Spincemaille P, Avestimehr AS, Wang Y. Accuracy of the Morphology Enabled Dipole Inversion (MEDI) Algorithm for Quantitative Susceptibility Mapping in MRI. *IEEE Trans Med Imaging* 2012;31(3):816–824.

41. Straub S, Schneider TM, Emmerich J, et al. Suitable reference tissues for quantitative susceptibility mapping of the brain. *Magn Reson Med* 2017;78(1):204–214.
42. Prashanth LK, Sinha S, Taly AB, Vasudev MK. Do MRI Features Distinguish Wilson's Disease from Other Early Onset Extrapyrimalidal Disorders? An Analysis of 100 Cases. *Mov Disord* 2010;25(6):672–678.
43. Lee JH, Yang TI, Cho M, Yoon KT, Baik SK, Han YH. Widespread cerebral cortical mineralization in Wilson's disease detected by susceptibility-weighted imaging. *J Neurol Sci* 2012;313(1-2):54–56.
44. Fritsch D, Reiss-Zimmermann M, Trampel R, Turner R, Hoffmann KT, Schafer A. Seven-tesla magnetic resonance imaging in Wilson disease using quantitative susceptibility mapping for measurement of copper accumulation. *Invest Radiol* 2014;49(5):299–306.
45. Dusek P, Bahn E, Litwin T, et al. Brain iron accumulation in Wilson disease: a post mortem 7 Tesla MRI - histopathological study. *Neuropathol Appl Neurobiol* 2017;43(6):514–532.
46. Benjamini Y, Yekutieli D. The control of the false discovery rate in multiple testing under dependency. *Ann Statistics* 2001;29(4):1165–1188.
47. Spincemaille P, Anderson J, Wu G, et al. Quantitative Susceptibility Mapping: MRI at 7T versus 3T. *J Neuroimaging* 2020;30(1):65–75.
48. Andersen K, Sudmeyer M, Saleh A. Cerebral imaging for Wilson disease. *Rofo-Fortschritte Auf Dem Gebiet Der Rontgenstrahlen Und Der Bildgebenden Verfahren* 2007;179(3):225–233.
49. Xu B, Liu T, Spincemaille P, Prince M, Wang Y. Flow compensated quantitative susceptibility mapping for venous oxygenation imaging. *Magn Reson Med* 2014;72(2):438–445.
50. Wisnieff C, Ramanan S, Olesik J, Gauthier S, Wang Y, Pitt D. Quantitative susceptibility mapping (QSM) of white matter multiple sclerosis lesions: Interpreting positive susceptibility and the presence of iron. *Magn Reson Med* 2015;74(2):564–570.
51. Chen W, Gautier SA, Gupta A, et al. Quantitative Susceptibility Mapping of Multiple Sclerosis Lesions at Various Ages. *Radiology* 2014;271:183–192.
52. Barbosa JHO, Santos AC, Tumas V, et al. Quantifying brain iron deposition in patients with Parkinson's disease using quantitative susceptibility mapping, R2 and R2*. *Magnetic Resonance Imaging* 2015;33(5):559–565.
53. Murakami Y, Kakeda S, Watanabe K, et al. Usefulness of Quantitative Susceptibility Mapping for the Diagnosis of Parkinson Disease. *American Journal of Neuroradiology* 2015;36(6):1102–1108.
54. Liu T, Khalidov I, de Rochefort L, et al. A novel background field removal method for MRI using projection onto dipole fields (PDF). *NMR Biomed* 2011;24(9):1129–1136.
55. Schafer A, Forstmann BU, Neumann J, et al. Direct visualization of the subthalamic nucleus and its iron distribution using high-resolution susceptibility mapping. *Human Brain Mapping* 2012;33(12):2831–2842.
56. Li G, Zhai G, Zhao X, et al. 3D texture analyses within the substantia nigra of Parkinson's disease patients on quantitative susceptibility maps and R2(*) maps. *Neuroimage* 2019;188:465–472.

Supporting Data

Additional Supporting Information may be found in the online version of this article at the publisher's web-site.

SGML and CITI Use Only
DO NOT PRINT

Author Roles

(1) Research project: A. Conception, B. Organization, C. Execution; (2) Statistical Analysis: A. Design, B. Execution, C. Review and Critique; (3) Manuscript: A. Writing of the first draft, B. Review and Critique.

G. Li: 1A, 1B, 1C, 2A, 2B, 2C, 3A, 3B.

R. Wu: 1B, 1C, 3B.

R. Tong: 1C, 3B.

B. Bo: 1B, 1C, 3B.

Y. Zhao: 1C, 3B.

K. Gillen: 1A, 3B.

P. Spincemaille: 1A, 3B.

Y. Ku: 2B, 2C.

Y. Du: 1A, 3B.

Y. Wang: 1A, 3B.

X. Wang: 1A, 1B, 2A, 2C, 3B.

J. Li: 1A, 1B, 2A, 2C, 3B.